Materials Today Bio 20 (2023) 100678

Contents lists available at ScienceDirect

Materials Today Bio

journal homepage: www.journals.elsevier.com/materials-today-bio

# Glucose-driven transformable complex eliminates biofilm and alleviates inflamm-aging for diabetic periodontitis therapy

Rongbing Tang [1,*], Yanrong Ren [1], Yueting Zhang [1], Mengying Yin, Xinyu Ren, Qiangyuan Zhu, Cen Gao, Wei Zhang, Guangxiu Liu [**], Bin Liu [***]

*School of Stomatology, Lanzhou University, Lanzhou, 730000, China*

ARTICLE INFO

*Keywords:*
Transformable complex
Hyperglycemia
Periodontitis
Biofilm penetration
Imflamm-aging

ABSTRACT

Diabetic periodontitis is a major complication of diabetes, which has a deep involvement in teeth loss and more serious systematic diseases, including Alzheimer's disease, atherosclerosis and cancers. Diabetic periodontitis is difficult to treat because of recalcitrant infection and hyperglycemia-induced tissue dysfunction. Current treatments fail to completely eliminate infection due to the diffusion-reaction inhibition of biofilm, and ignore the tissue dysfunction. Here, we design a glucose-driven transformable complex, composed of calcium alginate (CaAlg) hydrogel shell and Zeolitic imidazolate framework-8 (ZIF-8) core encapsulating Glucose oxidase (GOx)/Catalase (CAT) and Minocycline (MINO), named as CaAlg@MINO/GOx/CAT/ZIF-8 (CMGCZ). The reaction product of glucose-scavenging, gluconic acid, could dissolve ZIF-8 core and transform CMGCZ from inflexible to flexible, facilitating the complex to overcome the diffusion-reaction inhibition of biofilm. Meanwhile, reduced glucose concentration could ameliorate the pyroptosis of macrophages to decrease the secretion of pro-inflammatory factors, thereby reducing inflamm-aging to alleviate periodontal dysfunction.

## 1. Introduction

Periodontitis, especially in diabetic patients, leads to substantial resorption of alveolar bone and has even been implicated in numerous systematic diseases, such as Alzheimer's disease, atherosclerosis and a list of cancers, thus threatening human health worldwide [1–3]. Periodontitis in diabetic patients is compromised because of tissue dysfunction and recalcitrant infection [4–6]. Current treatments of periodontitis include supra/subgingival scaling, application of antibiotics and periodontal surgery [7,8]. However, the majority of these treatments not only fail to effectively decrease bacteria burden, but also are unable to correct tissue dysfunction. Therefore, the development of novel strategies combined with inhibiting infection and repairing tissue dysfunction is key to clinical success. Hyperglycemia, a hallmark of diabetes, is mainly responsible for diabetes-associated dysfunction through inducing inflamm-aging which is characterized by chronic inflammation and cellular senescence [9–12]. The primary modulator of inflamm-aging is macrophage in periodontic tissue. Hyperglycemia coerces macrophages into a pyroptosis state by directly increasing the expression and the phosphorylation of NLRC4 (*p*-NLRC4) [13–15]. The excessive *p*-NLRC4 activates downstream Caspase-1 to cleave gasdermin D (GSDMD) to liberate its N-terminal domain, which is responsible for forming pore structure on the cell membrane [16–19]. The GSDMD-associated pores disrupt the integrity of the cell membrane and interfere with osmotic potential, eventually causing pyroptosis. The pyrophoric macrophage is prone to develop a persistent pro-inflammatory phenotype, referred to as senescence-associated secretory phenotype (SASP), thereby secreting pro-inflammation factors, such as IL-1$\beta$, IL-6 and TNF- $\alpha$ [19]. A substantial pro-inflammatory cytokine is released toward surrounding tissue from the cytoplasm of pyrophoric macrophages through GSDMD-associated pores [16–19]. These pro-inflammatory cytokines induce the senescence of surrounding fibroblasts, which is responsible for synthesizing collagen to fabricate periodontal ligament, the most important supporting structure of teeth. The senescence-induced decline of proliferation and viability of fibroblasts in gingiva would compromise the function of the periodontal ligament, and eventually led to severe

* Corresponding author.
** Corresponding author.
*** Corresponding author.
*E-mail addresses:* tangrb@lzu.edu.cn (R. Tang), liugx@lzb.ac.cn (G. Liu), liubkq@lzu.edu.cn (B. Liu).
[1] These authors contributed equally to this work.

https://doi.org/10.1016/j.mtbio.2023.100678
Received 16 February 2023; Received in revised form 15 May 2023; Accepted 19 May 2023
Available online 25 May 2023

periodontitis [20–22].

In addition to the periodontal tissue dysfunction caused by inflamm-aging, recalcitrant infection is another intractable problem of diabetic periodontitis [23,24]. Oral bacteria spontaneously adhere to the surface of the tooth and are embedded in a self-produced matrix of extracellular polymeric substances, eventually forming a spatially heterogeneous ecosystem, called as dental plaque biofilm [23]. Due to a sophisticated network structure with intricately electrostatic distribution, biofilm can attenuate the activity of antibacterial substances through "diffusion--reaction inhibition", which involves static chelation, enzymatic degradation and steric hindrance, thereby leading to the failure of clinical treatment [24,25]. To overcome the diffusion-reaction inhibition for antibacterial substances, scientists have developed various kinds of nanomaterials, such as polymer micelles, metal nanoparticles, and metal-organic frameworks (MOFs), what has been widely explored as delivery platforms [26–38]. According to previous reports [39–43], MOFs (1D, 2D, 3D and $0D^{+}$) are widely applied in the field of enzyme immobilization, endowing enzyme considerable stability and excellent catalysis ability. Among them, enzyme immobilized with 1D and 2D structures MOFs were prone to be inactivated by external stimuli, and $0D^{+}$ structure MOFs was difficult to synthesize. MOFs with 3D structure may be more suited to the immobilization of enzyme due to great chemo-/machinal stability, large pore size and specific surface area. In situ immobilization was the most common method to use MOFs in enzyme immobilization field. In detail, enzymes were used as the core or inducing site and finally forms a stable MOF layer around enzymes, thus required a gentle synthesis condition [39]. Zeolitic imidazolate framework-8 (ZIF-8), a kind of MOFs, has garnered the most attention, attributed to its ultra-high porosity, negligible cytotoxicity, high thermal and chemical stability and low cost [44]. ZIF-8 is synthesized in a gentle condition, *e.g.* room temperature, aqueous solution, which is different from most other MOFs that required hash synthesis conditions. In addition, a protonation of 2-methylimidazole under acidic conditions impairs the coordination between it and $Zn^{2+}$, resulting in the collapse of ZIF-8 and the release of guest molecules in acid conditions. Depending on these advantages, ZIF-8 has been wildly applied in the field of precision medicine, including targeted delivery and pH-responsive release, especially for enzymes [45–47]. Cui et al. encapsulated Glucose oxidase (GOx) and Catalase (CAT) with ZIF-8 through in situ immobilization successfully, and the enzymes all exhibited considerable activity [42,43].

In this study, we constructed a glucose-driven transformable complex, composed of calcium alginate (CaAlg) hydrogel shell and ZIF-8 core encapsulating GOx, CAT and Minocycline (MINO), named CaAlg@MINO/GOx/CAT/ZIF-8 (CMGCZ) (Scheme 1a). When CMGCZ was injected locally in the gingival sulcus, the CMGCZ complex could exploit glucose to generate gluconic acid by GOx/CAT for degrading the ZIF-8 core. After the degradation begins, the hydrogel shell and remaining ZIF-8 core were incompetent to keep the rigidity of the complex, causing the complex to become flexible, including changeable shape and inconstant hydrodynamic diameter, to enter the top layer of biofilm (Scheme 1b). As the depth of penetration increases, the surrounding, acidification gradually deteriorates in the biofilm, accelerating the degradation of ZIF-8 to promote the biofilm penetration of the complex (Scheme 1c). In the process of ZIF-8 degradation, MINO was released sustainably for bacteria-killing through the whole biofilm. Meanwhile, hydrogen peroxide ($H_2O_2$), the noxious product of glucose degradation, was eliminated by CAT to guarantee the biosafety of CMGCZ. As the existence of residual hydrogel shell, GOx/CAT was

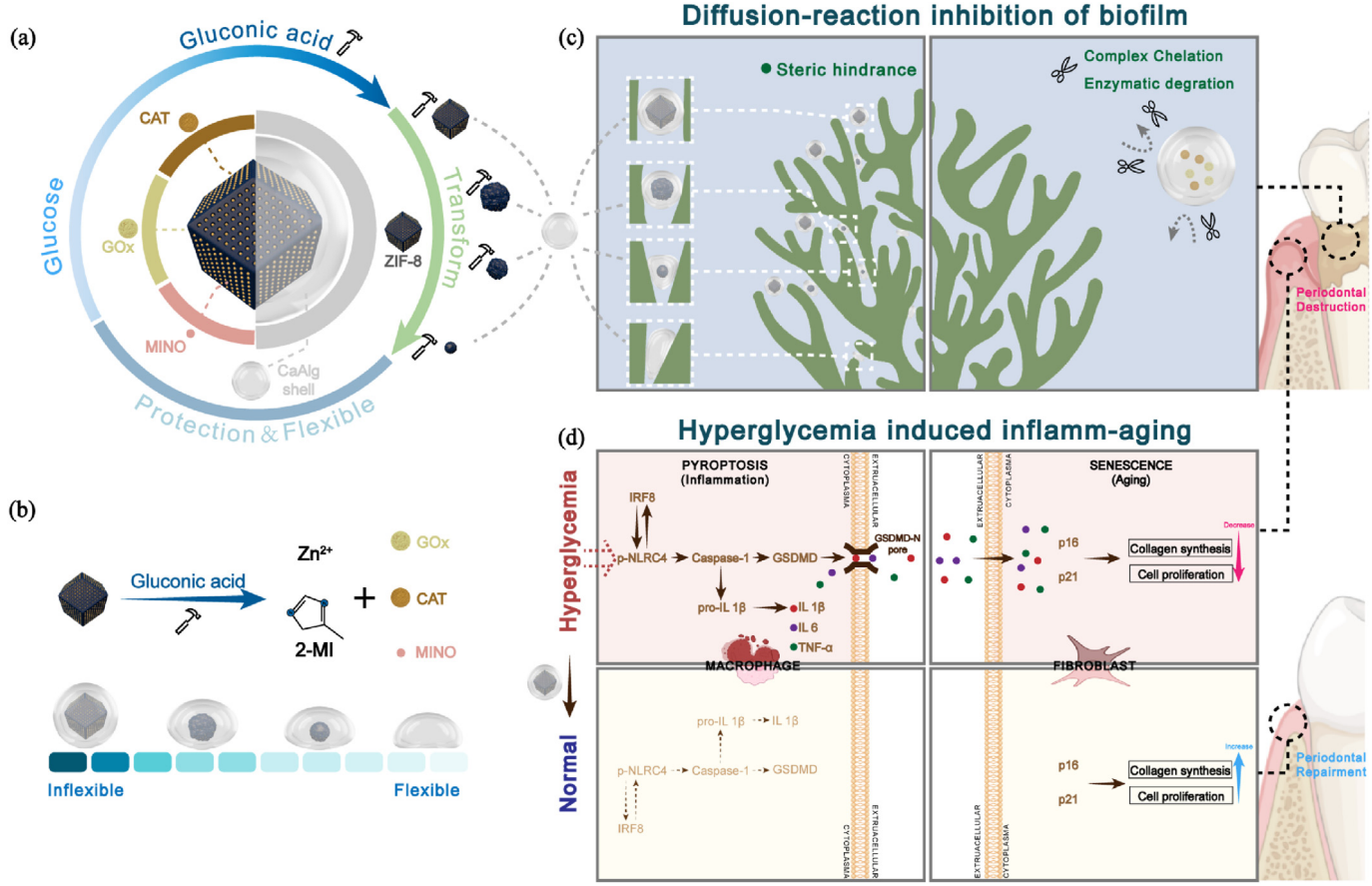


**Scheme 1.** Schematic illustration described (a) the composition of CMGCZ, (b) the mechanisms of ZIF-8 degradation and the rigidity of CMGCZ at different stages, (c) schematic showed the ability of penetration and protection about CMGCZ in biofilm and (d) the proposed anti-hyperglycemia induced inflamm-aging mechanisms of CMGCZ. Artwork in this Scheme was partially created with BioRender.com.

protected from the diffusion-reaction inhibition of biofilms, such as static chelation, enzymatic degradation and steric hindrance. Furthermore, the glucose-scavenging would ameliorate the pyroptosis of macrophages to decrease the secretion of pro-inflammatory factors, thereby reducing inflame-aging to alleviate the dysfunction of periodontal tissue (Scheme 1d). The novel strategy combined inhibiting infection and alleviating tissue dysfunction provided a promising therapy for diabetic periodontitis.

## 2. Materials and methods

### 2.1. Materials

2-Methylimidazole was obtained from Shanghai Aladdin Biochemical Co.,Ltd; Zinc acetate dihydrate was obtained from Shanghai Macklin Biochemical Technology Co., Ltd; Calcium chloride and Alginic acid sodium salt were obtained from Sigma Aldrich Chemical Co. LLC; Minocycline Hydrochloride was obtained from Hangzhou Xiaoyou Biotechnology Co.,Ltd; Glucose oxidase and Catalase were obtained from Beijing Solarbio Science & Technology Co., Ltd.

### 2.2. Preparation of CMGCZ

One-step synthesis was used in preparation of CMGCZ. In detail, $(CH_3COO)_2Zn$ (21.95 mg), 2-methylimidazole (32.8 mg), MINO (20 mg), CAT (300 μg/mL) and GOx (100 μg/mL) were dissolved in MilliQ water (20 mL) and stirred at 500 rpm for 12 h. Then collected the products by centrifuging and washing 3 times using MilliQ water, and stirred again with 5% $Ca^{2+}$ solution for 30 min to absorb $Ca^{2+}$. After absorbing, the products were harvested (8000 rpm centrifugation, 10 min, 3 times washing) and resuspended by MilliQ water, and 2.5% sodium alginate were added. The mixture was stirred at 500 rpm for 3 h, and centrifugated (8000 rpm, 10 min, 3 times washing) to obtain CMGCZ. As for fluorescence experiment, we introduced RBITC-bovine serum albumin (BSA) during the One-pot synthesis to labeled the core of complex with RBITC, and used FITC-NaAlg to labeled CaAlg shell with FITC.

### 2.3. Characterization of CMGCZ

Transmission Electron Microscope (TEM) and Energy Dispersive Spectroscopy (EDS) element mapping results were obtained on Tecnai F30 Transmission Electron Microscope. Confocal Laser Scanning Microscope (CLSM) images was obtained on Olympus FV3000 Confocal laser scanning microscope. Hydrated particle size was detected by dynamic light scattering (DLS) in Brookhaven 90Plus Pals. XRD spectra was taken on X-Ray Diffractometer (Rigaku, D/MAX-200, Japan). FT-IR spectra was obtained from NICOLET NEXUS 670.

### 2.4. Glucose-driven deformation assay

CMGCZ was dispersed in phosphate buffered saline (PBS) contained 5 mM、15 mM and 35 mM glucose for 1 h. After dialyzed for 48 h, dropped onto the Carbon support film and observed by TEM.

### 2.5. Encapsulation rate of enzymes and MINO

The encapsulation rate of enzymes was tested based on previous work [41,48]. In brief, the supernatant of preparation mixture of CMGCZ was collected by centrifugation, and the encapsulation rate of enzymes was evaluated using Eq. (1).

$$\text{Encapsulation rate}\% = \frac{(m - C1V1)}{m} \times 100 \quad (1)$$

Here, m (mg) represents the initial mass of enzymes added to the preparation mixture of CMGCZ; $C_1$ (mg/mL) and $V_1$ (mL) represents the concentration of enzymes and the volume of supernatant, respectively. As for MINO, CMGCZ was treated with pH 5.0 condition for 1 h to release all encapsulated MINO, and the encapsulation rate of MINO was calculated by Eq. (2):

$$\text{Encapsulation rate}\% = \frac{Me}{Mi} \times 100 \quad (2)$$

Me (mg) and Mi (mg) are the mass of encapsulated MINO and initial amount of MINO (20 mg) added at the preparation stage of CMGCZ, respectively.

### 2.6. Oral mixed bacteria and dental plaque biofilm culture in vitro

Oral mixed bacteria was obtained from periodontal pocket in patients with moderate/severe periodontitis in Hospital of Stomatology Lanzhou University, all participants signed the informed consent and fully understood the research purpose, and all experiments were approved by the Clinical Science Research Ethics Committee of School of Stomatology of Lanzhou University (LZUKQ-2021-043). The extracted plaque was cultured and passaged in anaerobic workstation (GeneScience, AG300, USA) with BHI medium. All patients were informed and in advanced of dental plaque bofilm removal. Dental plaque biofilm was cultured on Polycarbonate Membrane (PM) and tooth slices. In detail, oral mixed bacteria was added by drops onto the center of sterilized-PM, and bacteria-loaded PM was put on BHI agar medium and cultured in biochemical incubator at 37 °C for 7 days with 200 μL prepared oral mixed bacteria suspension (~$1x10^6$ CFU/mL) added per day.

Experimental teeth were collected from Hospital of Stomatology Lanzhou University. Teeth were sterilized by 75% alcohol, and then crowns were cut into 1–2 mm tooth slices by slicer (Veiyee, Laizhou). Slices were co-cultured with 2 mL oral bacteria (~$1x10^6$ CFU/mL) in a 24-well plate for 7 days after sterilized. The culture medium was changed every day. In detail, 1 mL of culture medium was extracted and discarded, and 1 mL fresh BHI was added to the mixture.

### 2.7. Observation of penetration about CMGCZ in dental plaque biofilm

FITC-Conchaiavalin A (ConA) was used to label the dental plaque biofilm in vitro (FITC-dental plaque biofilm). In detail, 50 μg/mL FITC-ConA was co-cultured with dental plaque biofilm at 37 °C in the dark for 30 min, and then washed three times with PBS. Then we labeled RBITC to CMGCZ through the introduction of RBITC-BSA during the One-pot synthesis. In glucose concentration variable group, RBITC-CMGCZ, treated with 0, 5, 15 and 35 mM glucose, was co-cultured with FITC-dental plaque biofilm for 60 min, then sliced dental plaque biofilm by frozen slicer (Leica CM1900, Germany) and placed on glass slides for CLSM observation. In the time variable group, untreated-RBITC-CMGCZ was co-cultured with FITC-dental plaque biofilm for 15min, 30 min, 60 min and 90 min, respectively, and then sliced dental plaque biofilm as above for CLSM observation.

### 2.8. The penetrate ability of glucose-treated CMGCZ in agar

1 mL, 2 mg/mL RBITC-CMGCZ was dispersed in various glucose concentration (5, 15, 35 mM glucose) for 30 min, and then dropped the mixture into Oxford Cups which were placed on the top of agar. After 60 min, the Oxford cups were removed, and cut CMGCZ-covered areas of the agar vertically into slices. CLSM was used to observe the vertical section of agar below the CMGCZ-covered area to evaluate the penetrate ability of glucose-treated CMGCZ in agar.

### 2.9. Enzyme activity assay

Certain amount of GOx samples and acid-treated CGCZ (pH = 5, 1 h) were added into 20 mL PBS contained 4% glucose at 37 °C for 5 h, respectively. The D-glucose concentration was detected by a Glucose

Content Assay Kit (Boxbio, Beijing). As for CAT, certain amount of CAT samples and acid-treated CGCZ (pH = 5, 1 h) were added into 20 mL PBS contained 0.33 M $H_2O_2$ at 30 °C for 5 h, respectively, and the $H_2O_2$ content was detected by a $H_2O_2$ Content Assay Kit (Solarbio, Shanghai).

The activity recovery of GOx was calculated by Eq. (3) based on previous studies [42].

$$\text{Activity recovery}\% = \frac{\text{Ar}}{\text{Af}} \times 100 \quad (3)$$

Ar (U) and Af (U) were the enzyme activity of released GOx and certain amount of free GOx samples, respectively.

### 2.10. GOx activity detection assay

Glucose Content Assay Kit were used to evaluate the activity of GOx. We built ZIF-8/GOx/CAT (ZGC), CaAlg@GOx/CAT/ZIF-8 (CGCZ) to aviod the influence of yellow substance minocycline. According to the encapsulation rate of enzymes, we dispersed GOx, ZGC and CGCZ in 20 mL PBS contained 5, 15, 35 mM glucose, and incubated in 37 °C with shaking. 1 mL of mixture was drawed in 2 mL centrifuge tube at each time point, and 95 °C bath heating for 10 min. After bath heating, the mixture was centrifuged at 8000 rpm for 5 min, and the content of glucose in supernatant was detected by Glucose Content Assay Kit and microplate reader.

### 2.11. CAT activity detection assay

Hydrogen peroxide content assay kit was used to evaluate the enzymatic activity of CAT. CaAlg@GOx/ZIF-8 (CGZ) and CGCZ was structured for comparison. CGZ (2 mg/mL) and CGCZ (2 mg/mL) were incubated with PBS containing 15 mM and 35 mM glucose at 37 °C, respectively. 1 mL of the mixture was taken at each time point for detection.

### 2.12. Release of minocycline

3 mL PBS (5, 15 and 35 mM glucose concentration) with CMGCZ (2 mg/mL) were placed into dialysis bag, and then the dialysis bag were placed into a 50 mL centrifuge tube containing 20 mL PBS (pH = 7). The whole system was bathed in a 37 °C, and 3 mL PBS was taken from the centrifuge tube according to the planned time point and added the same volume. Extracted PBS was used to detect minocycline at 350 nm with an ultraviolet spectrophotometer (Analytik Jena, SPECORD 50plus, Germany) to assess minocycline concentration.

### 2.13. Antibacterial effect in vitro

Evaluation of minimum inhibitory concentration (MIC). CMGCZ was diluted in 96-well plates using the gradient dilution method. Oral mixed bacteria was diluted $10^6$ times when cultured to an appropriate concentration (~1x$10^6$ CFU/mL), and then added into the 96-well plate. Then the 96-well plate were placed in an incubator (PEIYIN, SHP-150PY, Shanghai) at 37 °C for 12 h, and detected at 600 nm by a microplate reader (TECAN, Infinite M200 Pro, Swiss) to evaluate the growth of bacteria.

### 2.14. Live/dead bacterial double staining in dental plaque biofilm

Dental plaque biofilms on teeth slices were stained using Live/Dead Bacterial Double Staining Kit according to the recommended procedures. Dental plaque biofilms were co-cultured with CMGCZ at various concentrations under 35 mM glucose, and stained at 24, 48 and 72 h. CLSM was used to observe the distribution of live and dead bacteria.

### 2.15. Destruction of dental plaque biofilm

Dental plaque biofilms on teeth slices was stained by FITC-ConA. Dental plaque biofilms were co-cultured with CMGCZ at various concentrations, and stained at 24, 48 and 72 h under 35 mM glucose. CLSM was used to observe the integrity of dental plaque biofilms.

### 2.16. Phagocytosis of RAW264.7 for various complexes

Macrophages was stained with CFSE and cultured in 12-well plates, and 100 μg/mL various RBITC-complex was added and co-cultured with macrophages for different time. CLSM was used to observe the phagocytosis of RAW264.7 for various complexes.

### 2.17. The CCK8 assay

Macrophages was cultured in 96-well plates, and various concentration of CMGCZ was added and co-cultured with macrophages in 37 °C, 5% $CO_2$ for 24h and detected at 450 nm by a microplate reader (TECAN, Infinite M200 Pro, Swiss).

### 2.18. Evaluation of cytokines by ELISA

Supernatant of macrophages cultured in each groups (5 mM Glucose medium, 15 mM Glucose medium, 35 mM Glucose medium, 15 mM Glucose + CMGCZ medium and 35 mM Glucose + CMGCZ medium) was collected and centrifugated (481 g, 5 min) to remove cell fragments. All samples were added in the Elisa kit and react at 37 °C for 30 min. Then washed five times with washing solution, added HRP-Conjugate reagent, and incubated at 37 °C for 30 min. Next, washed for 5 times, added Chromogen Solution A and B in order, and then incubated for 10 min at 37 °C. Finally, stop solution was added, and read absorbance results at 450 nm within 15 min.

### 2.19. Western Blotting assay

RAW264.7 cells were treated by lysis buffer (R0010, Solarbio) contained protein phosphatase inhibitor (P1260, Solarbio). Protocol recommended was followed, and 15 mg of protein from each sample was subjected to 10% SDS-PAGE and transferred to nitrocellulose membranes (Millipore, USA) by electroblotting. Nitrocellulose membranes were incubated in 4 °C shaking bed (ZHICHENG, Shanghai) overnight with primary antibodies against β-actin (1:1500, GB12001, Servicebio), GSDMD (1:1500), *p*-NLRC4 (1:1500, B7–B7, HUABIO), NLRC4 (1:1500, YT7243, Immunoway), Caspase-1 (1:1500, YT0652, Immunoway), IRF8 (1:1500), p16 (1:1500, B7241, Santa Cruz) and p21 (1:1500, B3478, Santa Cruz). After the incubating with primary antibodies, nitrocellulose membranes was incubated with secondary goat-anti-mouse (1:5000, RS0001, Immunoway) or goat-anti-rabbit (1:5000, RS0002, Immunoway) antibodies for 1–2 h at room temperature. The results were obtained by chemiluminescence imaging system (CLINX, ChemiScope 6100, Shanghai).

### 2.20. Animals

4-week-old Wistar rats were selected and purchased from Animal Experimental Center of Lanzhou University. All animal experimental protocols were performed strictly following the guidelines established by the Ethics Committee and the Institutional Animal Care and Use Committee of Lanzhou University (LZUKQ-2021-044).

### 2.21. Establishment of animal model

Wistar rats were used for experiments. After being fed with high fat diet (BOAIGANG, Beijing) for 4 weeks, Streptozocin (STZ, Solarbio) was injected at a dose of 35 mg/kg to establish a diabetic rat model. As for

periodontal model, rats were anesthetized by 3% sodium pentobarbital, and 4-0 sutures were soaked in oral mixed bacterial solution. The left maxillary first molars of rats were ligated with oral mixed bacterial-soaked sutures. Additionally, oral mixed bacterial solution was added to the ligation area, and the sutures were tightened with orthodontic ligation wire across onto it. After two weeks ligation, diabetic periodontal model was successfully established, then removed the sutures.

### 2.22. Statistical analysis

Data were present as means ± standard deviation (SD) in this article. One-way repeated-measures ANOVA with the LSD post hoc test was used to analyze the documents between experimental groups via Statistical Product and Service Solutions (SPSS), and statistical significance was considered as P value $< 0.05$.

## 3. Results and discussions

### 3.1. Preparation and characterization of complex

Fig. S1 showed the schematic illustration of the synthesis of CMGCZ, which was composed of a glucose-driven degradation core and a flexible hydrogel shell. The core of CMGCZ which is a ZIF-8 structure loaded guest substance (ZIF-8/MINO/GOx/CAT, ZMGC), was synthesized by the one-step method. According to previous studies [49], the gelation of CaAlg shell on the surface of CMGCZ was caused by the ionic binding of divalent cations and the G-block region of the alginate polymer. The ionic bridges between the two COO- groups on the G-block region and calcium ions formed a 3D network structure. In brief, as shown in Fig. S2a, ZIF-8 had a standard orthododecahedral structure with smooth surface, sharp edges and corners. In comparison, after forming CaAlg hydrogel shell on the surface, the morphology of particle became rough and blunt (Fig. S2b). After removing ZIF-8 core of CMGCZ by acid treatment, the CaAlg hydrogel shell exhibited thin walled vesicle-like structure (Fig. S2c).

The complex was analyzed using TEM coupled with EDS mapping to confirm the ZIF-8 crystal structure and core-shell structure. TEM revealed that ZMGC possesses a typical polyhedron morphology as ZIF-8 (Fig. S3) and has a narrow distribution in an average size of 407 ± 21 nm (Fig. 1a). After the adsorption of $Ca^{2+}$ ions, the edges of ZMGC became irregular, indicating that the minority $Zn^{2+}$ in ZIF-8 was replaced by $Ca^{2+}$ [50]. In comparison, CMGCZ displayed a typical core-shell structure with a uniform size of about 506 ± 26 nm, in which the dodecahedral core (ZMGC) was wrapped by a CaAlg hydrogel shell with a thickness of 99 ± 5 nm (Fig. 1a and b). Due to the solvent effect [51], complex showed a larger hydrodynamic diameter (573 ± 55 nm) measured by dynamic light scattering (DLS) (Fig. 1c). Compared with previous studies [52], CMGCZ could transform and reduce its own particle size by responding to the local periodontal environment of diabetic periodontitis, avoiding the potential nanotoxicity. To verify that CAT and GOx were immobilized in the CMGCZ, we labeled the enzyme composites (GOx/CAT) with RBITC-BSA and labeled the shell with CaAlg-FITC. As shown in Fig. 1d–e, a green fluorescence was wrapped around the red fluorescence, the colocalization ratio of red and green fluorescences was about 74.22%, confirming the enzyme composites was successfully encapsulated by CaAlg. In addition, the peak at 1630 $cm^{-1}$, 1650 $cm^{-1}$ and 3300 $cm^{-1}$ in Fourier transform infrared (FT-IR) spectra of CMGCZ also verified the existence of GOx, CAT, MINO and CaAlg shell in the complex (Fig. 1f) [43], which was consistent with the results of fluorescences and flow cytometry (Fig. 1d–e). The similar X-Ray Diffraction (XRD) patterns demonstrated the crystal structure of ZIF-8 was not affected by the incorporation of CaAlg, MINO, CAT and GOx (Fig. 1g). Zeta potentials of ZIF-8 was around +20 mV, and that of CMGCZ was at −20 mV (Fig. 1h). MINO could be encapsulated in MOFs through surface adsorption,

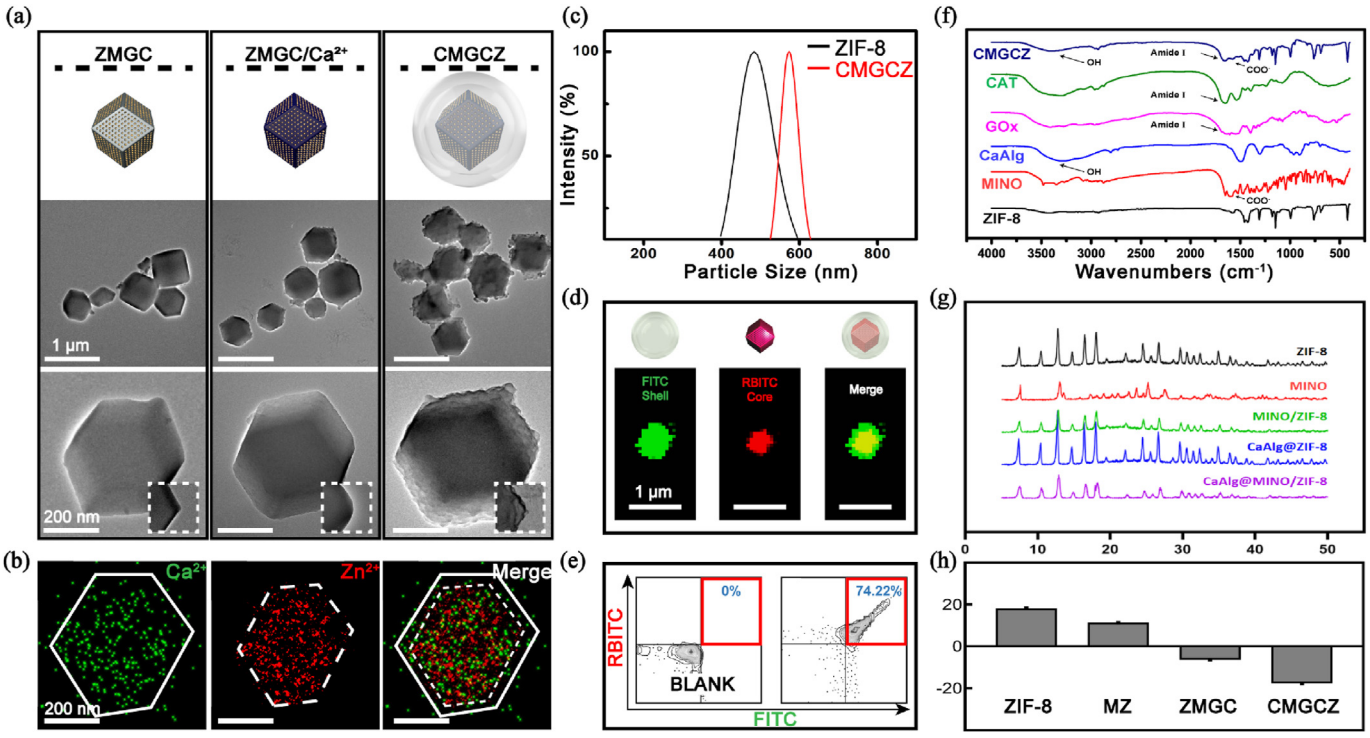


**Fig. 1.** Characterization of CMGCZ complex. (a) TEM images of ZMGC, ZMGC/$Ca^{2+}$ and CMGCZ. Insets showed the edge and corner of complex (scale bars: 1 μm and 200 nm). (b) EDS mapping images of CMGCZ, all images on a scale of 200 nm. (c) Hydrodynamic diameter of ZIF-8 and CMGCZ measured by DLS (means ± SD, n = 3). (d) CLSM images of CMGCZ, all images on a scale of 1 μm. (e) Images of Flow cytometry about CMGCZ. (f) FTIR characterization of ZIF-8, MINO, GOx, CAT, CaAlg, CMGCZ. (g) XRD spectra of ZIF-8, MINO, MINO/ZIF-8 (MZ), CaAlg@ZIF-8 (CZ) and CaAlg@MINO/ZIF-8 (CMZ). (h) Zeta characterization of ZIF-8, MZ, ZMGC and CMGCZ (means ± SD, n = 3).

inter-molecular force and so on [39]. The encapsulation rates of enzymes and MINO were also tested, and the results showed that the encapsulation rates were 90.12% and 7.13%, respectively. Compared with free enzyme, the activity recovery of immobilized enzyme was reached 70.26% (GOx) and 72.57% (CAT), indicating that the enzyme can restore most of catalytic activity and catalyze the substrate efficiently after release (Fig. S4). The storage modulus and loss modulus of CMGCZ suspension was also tested by rheometer. The results verified that the suspension remained liquid state, indicating that CMGCZ could be injected to the periodontal pocket by syringe (Fig. S5). In addition, Fig. S6 verified a good performance of injectability of CMGCZ.

### 3.2. Evaluation of glucose-driven transformation ability of CMGCZ in vitro

To evaluate the glucose-scavenging potential of CMGCZ in diabetic periodontitis therapy, we exposed CMGCZ to high glucose concentration containing a variety of reagents [53]. As shown in Fig. 2a–c, the glucose-scavenging activity of CGCZ almost approached that of free GOx, demonstrating the catalytic activity of GOx was impervious to the encapsulation of ZIF-8. Ascribing to gluconic acid, a reaction product of GOx-catalyzed glucose oxidation, the ZIF-8 gradually collapsed along with time and glucose concentration. TEM imaging revealed the structure of the ZIF-8 core of CMGCZ was gradually fragmented with exposure to high glucose, and disappeared after 30 min, while the hydrogel shell of the complex maintained integrity (Fig. 2d and e). Relying on the degradation of the ZIF-8 core and the flexibility of the hydrogel shell, the rigidity of the complex transformed from inflexible to flexible, endowing CaAlg@MINO/GOx/CAT (CMGC) with changeable shape, inconstant hydrodynamic diameter. As for $H_2O_2$, the noxious product of GOx, mediated glucose degradation, was eliminated effectively by CAT to avoid generating cytotoxicity (Fig. 2f).

To determine whether CMGCZ can overcome other challenges from the diffusion-reaction inhibition of biofilm, *e.g.* enzymatic degradation, we exposed CMGCZ to high glucose solution containing proteinase K (PK), which can hydrolyze and inactivate the GOx. The results showed glucose-scavenging activity of the complex with hydrogel shell did not be affected with PK, implying the retaining hydrogel shell build a barrier to avoid PK attacking enzyme composites (GOx/CAT) of the complex (Fig. 2g and h). Then, we conducted the colocalization analysis of the hydrogel shell and enzyme composites (GOx/CAT) after different degrees of ZIF-8 core collapse. Flow cytometry measurement (Fig. 2i) revealed the colocalization ratio of red fluorescence (RBITC, enzyme composites) signals and green fluorescence (FITC, CaAlg shell) signals in various treatments (glucose con. = 5 mM, 15 mM and 35 mM) was about to 91.21%, 87.68% and 85.84%, respectively (Fig. 2i). The CLSM imaging showed the red fluorescence was overlaid with green fluorescence, and the colocalization Pearson correlation coefficients of red and green fluorescence signals in each group were 0.9591, 0.9852, 0.981 and 0.952, respectively (Fig. 2j). The above results suggested that the CaAlg shell remains an integrity structure and encapsulates GOx/CAT against the enzymatic degradation in the biofilm.

To investigate whether the glucose-driven transformation of CMGCZ can overcome the steric hindrance of biofilm, RBITC labeled CMGCZ was added to the FITC-ConA labeled biofilm in the culture medium with varying concentrations of glucose (0–35 mM) [54,55]. 60 min after incubation, the biofilms were cryo embedded, sectioned, and analyzed by CLSM. After incubation with 5, 15, 35 mM glucose, the penetrated ability of CMGCZ represent a linear increase (23.75%, 56.5%, 69.62%, respectively) (Fig. 2k). In comparison, when the CMGCZ has exposed to 0 mM glucose, the penetrated ability of CMGCZ obviously decreased, indicating the transformation of CMGCZ was mainly driven by glucose (Fig. 2k). The penetration of CMGCZ in agar also showed similar trends (Fig. S7). The penetration depth of CMGCZ in 35 mM glucose, was increased from 26.9% to 83.47% along with time (Fig. 2l). Interestingly, CaAlg@MINO/ZIF-8 (CMZ), a complex without GOx, also diffused into parts of the biofilm, and the penetration depth of CMZ increases from 6.52% (15 min) to 49.5% (90 min), suggesting the local acidic environment of the biofilm also contributed to the collapse of ZIF-8, accelerating the glucose-driven transformation (Fig. 2m). The results confirmed that the transformation of CMGCZ endows CMGC with changeable shape and inconstant hydrodynamic diameter to traverse the inhomogeneous network structure of dental plaque biofilm.

### 3.3. Evaluation of antibacterial efficacy in vitro

In the penetration process of CMGCZ, the loaded MINO was gradually released along with the degradation of ZIF-8. To evaluate the release efficiency of MINO from CMGCZ in response to varying glucose concentrations, the absorption spectrum of released MINO in the supernatant was detected. The release of MINO exhibited a dependence on glucose concentration and time. The percentage of released MINO reached 25% within 90 min treated with 5 mM glucose. In comparison, in 15 and 35 mM glucose, MINO could release more than 50% and 75% within 90 min (Fig. 3a). A correlation matrix between MINO release and penetrated depth was depicted in Fig. S8 indicating the released MINO achieved the complete coverage of any position in the biofilm to eradicate sequestered bacteria. In order to investigate the antibacterial activity for planktonic bacteria of CMGCZ, the minimum inhibitory concentration (MIC) and minimum bactericidal concentration (MBC) of the complex on oral bacteria, which was collected from periodontitis patients, confirmed the bactericidal effect of CMGCZ (Fig. 3b–d). CMGCZ in 2 mg/mL glucose Brain-Heart Infusion (BHI) broth showed a better bactericidal effect than in 0 mg/mL glucose BHI broth, demonstrated that high glucose promoted the release of MINO. Next, we conducted the Live/Dead bacterial double staining to evaluate the bactericidal activity of CMGCZ for dental plaque biofilm under 35 mM glucose. Oral bacteria were cultured on the surface of tooth slices to emulate dental plaque biofilm (Fig. S9). The results showed the addition of CMGCZ pronouncedly kills bacteria sequestered in the biofilm, and the antibacterial efficiency was correlated to the administration dose and co-incubating time (Fig. 3e). Moreover, scanning electron microscope (SEM) imaging displayed that the surface of the tooth slice was flat and clean, emphasizing that CMGCZ was able to eradicate biofilm structure (Fig. 3f). Then we utilized FITC-ConA to bind polysaccharides of EPS for disclosing the biofilm. 72 h after treatment with CMGCZ dose in a range from 0 *mg*/mL to 2 *mg*/mL, only a few residual biofilm was observed on the tooth slice incubated with 2 *mg*/mL CMGCZ (Fig. 3g). The results were in a manner analogous to that observed in the Live/Dead staining analysis. In conclusion, compared with other studies [56], CMGCZ could not only release MINO to play a bactericidal role, but also could consume glucose in periodontal microenvironment to inhibit rampant bacterial growth conditions.

### 3.4. Evaluation of anti-pyroptosis and anti-senescence efficacy in vitro

To determine the effect of CMGCZ on inflamm-aging associated inflammation in diabetes periodontitis, the macrophage (RAW264.7), a common immunomodulatory cell, was cultured in cell medium with high glucose levels to emulate hyperglycemia. Macrophages (CFSE, green) engulfed a majority of ZIF-8 NPs (RBITC, red) within 12 h, while the complex with CaAlg shell still distribute in the extracellular space and avoid the clearance of macrophages, thus extending the time of complex effect (Fig. 4a). The CCK-8 assay results indicated CMGCZ did not affect the activity of cells cultured (Fig. 4b). We further examined the hemocompatibility of CMGCZ and the results showed that CMGCZ could remain stable and would not cause hemolysis (Fig. S10). In order to mimic hyperglycemia, we used cell culture medium with 35 mM glucose as previously reported [53]. Noteworthily, when macrophages were exposed to 35 mM glucose, cells showed lower cell viability than in 5 and 15 mM glucose (Fig. S11). According to previous reports, high glucose concentration impairs cellular activity by means of inducing programmed cell death, such as pyroptosis and apoptosis [12,13]. As shown in Fig. 4c, a large number of macrophages exposed to high glucose

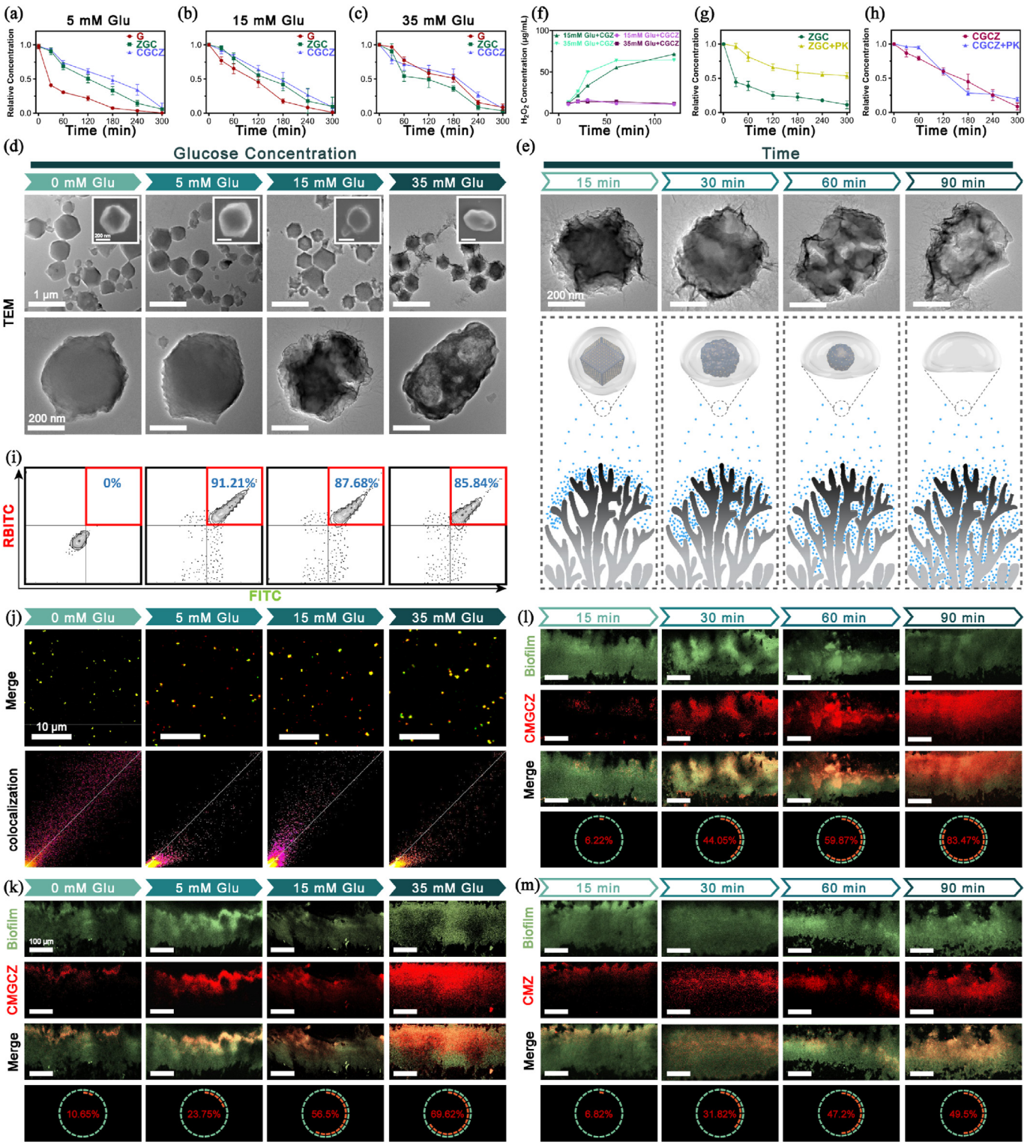


**Fig. 2.** Evaluation of glucose-driven transformation ability of CMGCZ in vitro. The enzyme activity of GOx in CMGCZ dispersed in PBS contained (a) 5 mM glucose, (b) 15 mM glucose and (c) 35 mM glucose (means ± SD, n = 3). (e) TEM images of CMGCZ treated with 0, 5, 15, and 35 mM glucose. Insets showed SEM images of CMGCZ treated with 0, 5, 15, and 35 mM glucose (scale bars: 1 μm and 200 nm). (e) The time-variable transformation of CMGCZ in 35 mM glucose (scale bar: 200 nm). (f) The levels of $H_2O_2$ in PBS contained CGZ+15 mM glucose, CGCZ +15 mM glucose, CGZ+35 mM glucose, CGCZ+35 mM glucose (means ± SD, n = 3). The enzyme activity of GOx in PBS contained (g) ZGC+35 mM glucose with or without PK treatment, (h) CGCZ+35 mM glucose with or without PK treatment (means ± SD, n = 3). The results of (i) flow cytometry and (j) CLSM about CMGCZ treated by 0, 5, 15, and 35 mM glucose, scale bar: 10 μm. Penetration of (k) CMGCZ, (l) 35 mM glucose-treated CMGCZ in FITC-dental plaque biofilm. Scale bar: 100 μm. (m) Penetration of CMZ in FITC-dental plaque biofilm. Scale bar: 100 μm.

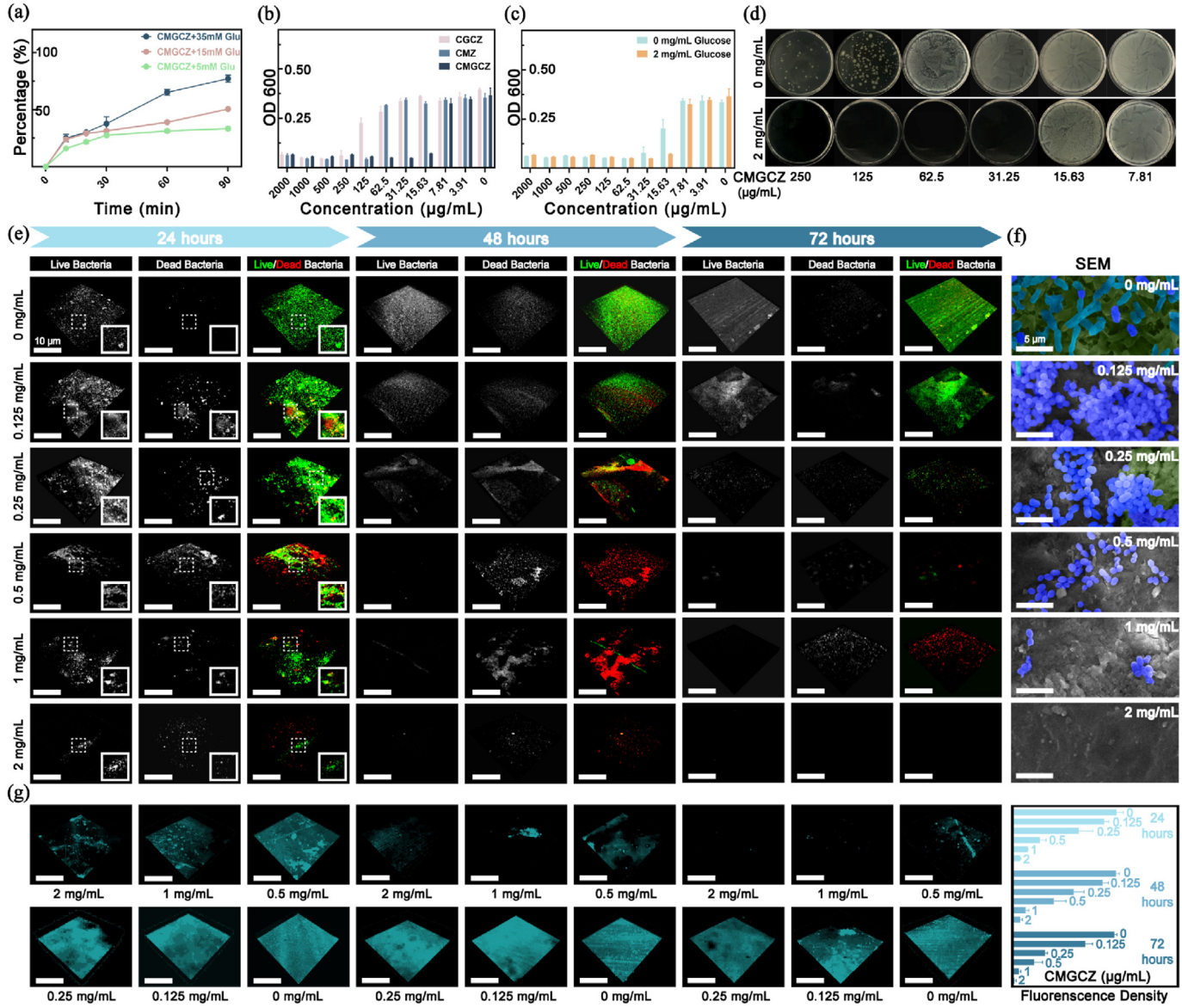


**Fig. 3.** The antibacterial aspects of CMGCZ. (a) MINO release capacity of CMGCZ treated with 5, 15 and 35 mM glucose (means ± SD, n = 3). (b) The minimum inhibitory concentration (MIC) of CGCZ, CMZ and CMGCZ against oral bacteria in 2 mg/mL glucose BHI broth (means ± SD, n = 5). (c) The MIC of CMGCZ against oral bacteria in 0 and 2 mg/mL glucose BHI broth (means ± SD, n = 5). (d) The MBC of CMGCZ against oral bacteria in 0 and 2 mg/mL glucose BHI broth. The CLSM images of dental plaque biofilm destruction ability about CMGCZ. (e) Live/Dead bacterial staining of dental plaque biofilm treated with various concentrations of CMGCZ (scale bar: 10 μm) and the (f) SEM images of 72-h-treated dental plaque biofilm on tooth slices. Scale bar: 5 μm. (g) FITC-conA staining of dental plaque biofilm treated with various concentrations of CMGCZ, scale bar: 10 μm.

exhibited membrane rupture (Q1, PI+, Annexin V FITC -), which was the characteristic of pyroptosis. Likewise, the expression level of GSDMD, a key marker of pyroptosis, gradually increased with increasing glucose concentrations, consist with other studies showing that high glucose activates macrophage pyroptosis. In comparison, the addition of CMGCZ significantly decreased pyrophoric macrophages exposed to 35 mM glucose, revealing CMGCZ prevents macrophages from pyroptosis. To decipher the mechanism of CMGCZ-inhibited pyroptosis, we detected the expression level of key proteins of the pyroptosis-associated signaling pathway in diabetic periodontitis, including NLRC4, IRF8 and Caspase-1. The western blot results revealed the expression and *p*-NLRC4, which is a pivotal target of high glucose-induced pyroptosis, were upregulated obviously in the macrophages exposed to 15 and 35 mM glucose. A similar trend was observed in the expression of IRF8, which is essential for the phosphorylation of NLRC4. In turn, the *p*-NLRC4 activated Caspase-1, which is able to cleavage the pore-forming protein GSDMD to liberate its N-terminal domain for rupturing cell membrane (Fig. 4d). Whereas the addition of CMGCZ decreased these protein levels of macrophages exposed to 15 and 35 mM glucose, verifying GMGCZ can facilitate macrophages avoiding high-glucose induced pyroptosis.

In the pyrophoric macrophages, the up-regulated *p*-NLRC4 activates NF-$\kappa$B, which contributes to generating massive pro-inflammatory factors by switching inflammatory pathways. In addition, the ruptured membrane of pyrophoric macrophages facilitates the release of pro-inflammatory cytokines to the extracellular microenvironment. As shown in Fig. 4e, CMGCZ treatment reduced the expression level of pro-inflammatory cytokines (IL-1$\beta$, IL-6 and TNF-$\alpha$) in the supernate of macrophages exposed to 15 mM and 35 mM glucose, manifesting that the suppression of pyroptosis by CMGCZ has the potential to alleviate chronic inflammation in periodontal tissue with inflamm-aging state (Fig. 4e–g).

Take into account that pyrophoric macrophages play a key role in

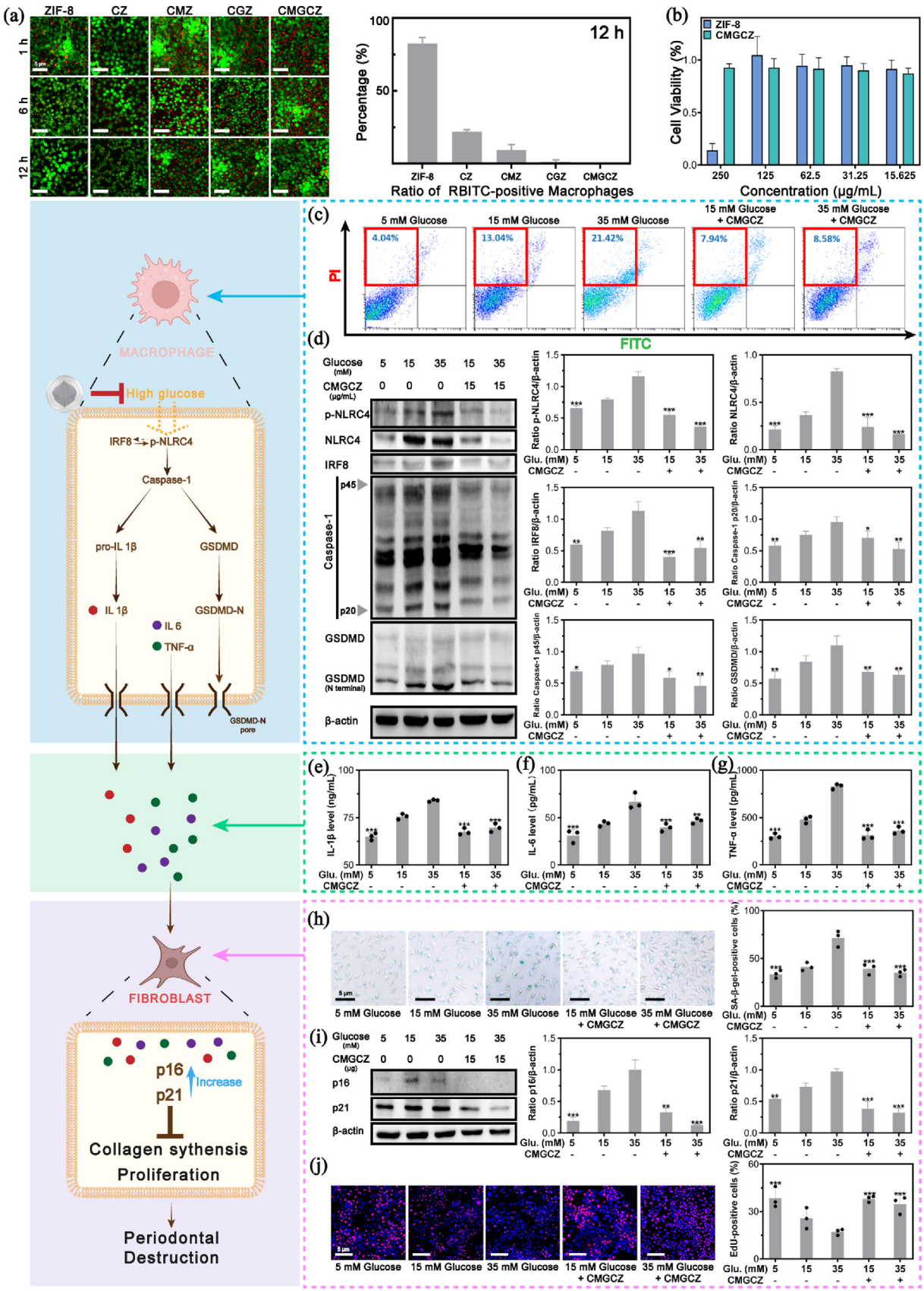


*(caption on next page)*

**Fig. 4.** Evaluation of *anti*-pyroptosis and anti-senescence efficiency of CMGCZ in vitro. (a) CLSM images of the phagocytosis of RAW264.7 for various complex (15 μg/mL), scale bar: 5 μm. (b) The biosafety of CMGCZ detected using the Cell Counting Kit-8 (CCK8) assay (means ± SD, n = 5). (c) The pyroptosis of RAW264.7 cultured in different conditions detected by flow cytometric analysis. (d) The expression levels of *p*-NLRC4, NLRC4, IRF8, Caspase-1, GSDMD and β-actin in RAW264.7 cultured in different conditions for 24 h detected using the Western Blotting assay. (e, f, g) Analysis the expression levels of IL-1β, IL-6 and TNF-α in different mediums using ELISA (15 μg/mL CMGCZ). Means ± SD, n = 3, * is $p < 0.05$, ** is $p < 0.01$, *** is $p < 0.001$. (h) The level of SA-β-gel in HGFs cultured with various condition mediums detected by SA-β-gel kit (scale bar: 5 μm, means ± SD, n = 3, * is $p < 0.05$, ** is $p < 0.01$, *** is $p < 0.001$). (i) The expression levels of p16, p21 and β-actin in HGFs cultured in different medium supernatant of RAW264.7 for 24 h showed by Western Blotting assay (means ± SD, n = 3, * is $p < 0.05$, ** is $p < 0.01$, *** is $p < 0.001$). (j) The cell proliferation of HGFs cultured in different medium supernatant of RAW264.7 for 24 h using Edu assay. Scale bar: 5 μm, means ± SD, n = 3, * is $p < 0.05$, ** is $p < 0.01$, *** is $p < 0.001$. Artwork in this Figure was partially created with BioRender.com.

paracrine senescence of Human Gingival Fibroblasts (HGFs) in the inflamm-aging state of periodontal tissue, HGFs was cultured in conditioned medium (CM) which derived from the supernatant of hyperglycemia-stimulated macrophages with different treatment. As depicted in Fig. 4h, the activity of SA-*β*-galactosidase (SA-*β*-gal), a canonical marker of cell senescence, significantly increased in HGFs cultured with CM from pyrophoric macrophages. The western blot results showed the expression of p16 and p21, which are associated with senescence-induced growth arrest, gradually increased after treating with various CM (Fig. 4i) [57]. In comparison, the expression levels of p16 and p21 were decreased significantly in CMGCZ-treated group, verifying that CMGCZ relieved the senescence of HGFs (Fig. 4i). Consequentially, the Edu assay demonstrated CMGCZ treatment reversed the senescence-induced growth arrest (Fig. 4j). Compared with previous works [58], CMGCZ could alleviate the inflamm-aging condition effectively in diabetic periodontitis, providing a novel treatment strategy.

### 3.5. Evaluation of periodontal therapeutic effect of CMGCZ in vivo

To determine the efficacious of CMGCZ in vivo, we established the rat model of diabetic periodontitis. A schedule of all procedures was presented in Fig. 5a. Rats fed a high fat diet (HFD) feeding for 4 weeks. After administrating streptozotocin (STZ), the blood glucose of rat progressively increased, and stabilized at 25–35 mM, confirming the rat had suffered from diabetes. Then we established a periodontitis rat model with the reported methods [9]. After the successful establishment of the above model, rats were treated with CMGCZ or other drugs for 3 weeks. Considering the frequent activities in mouths, rats were injected with CMGCZ or other drugs every 3 days. Then euthanized rats and harvested samples for further analysis. The micro-computed tomography (Micro-CT) analysis was performed to evaluate the bone resorption and neonatal formation of alveolar bone in the model rat with different treatments. The severe alveolar bone resorption nearby the cementoenamel junction was observed in periodontitis group (P), diabetic periodontitis group (DP) (Fig. 5b). The clinical first-line drug, Periocline (PERIO), slightly alleviate alveolar bone resorption in periodontitis + PERIO group (P + PERIO) and diabetic periodontitis + PERIO group (DP + PERIO), while CMGCZ treatment exhibited better therapeutic effect for periodontal rats and diabetic periodontal rats. The quantitative analysis of micro-CT images further revealed bone volume versus total volume (BV/TV), Trabecular Separation/Spacing (Tb.Sp) and Trabecular Thickness (Tb·Th) of rats treated with CMGCZ was superior to that in other groups (Fig. 5b). The results of hematoxylin and eosin (H&E) and Masson staining confirmed that CMGCZ promoted the repairment of periodontal tissue, represented the cementoenamel junction-alveolar bone crest (CEJ-ABC) distance of CMGCZ group reduced and the amount of collagen fibers increased significantly (Fig. 5c). Considering PERIO contains equivalent minocycline with CMGCZ, we assumed the glucose-scavenging and glucose-driven transformable ability reinforced the *anti*-biofilm efficiency of CMGCZ to protect periodontal tissues from bacterial infection.

To definite what role CMGCZ played in the inflammation in periodontal tissue (inflamm-aging state), gingival tissue of rats with various treatments was harvested for immunofluorescence staining analysis. As shown in Fig. 5d, the infiltrated macrophages (F4/80, green) were seldom observed in the CMGCZ group, which is similar to that in the control group, indicating CMGCZ can alleviate hyperglycemia-induced inflammation in periodontal tissue. To investigate whether CMGCZ decreases senescent cell burden in periodontal tissue (inflamm-aging state), we identified p16 and p21, both of which are the typical marks of the senescent cell. In the diabetic periodontitis group, numerous fluorescence of p16 and p21 were widely distributed in the gingival tissue consistent with the previous description that senescent cells are permanently withdrawn from the cell cycle and accumulated in the tissue along with time. Moreover, we found the cells expressed in p16 and p21 were localized next to macrophages (F4/80, green), indicating that the senescence is induced by the paracrine of pyrophoric macrophages. Whereas these proteins were only marginally expressed in the gingival tissue of the CMGCZ group, consistent with the results in cell experiments, manifesting CMGCZ is able to decrease hyperglycemia-induced inflamma-aging in periodontal tissue. In addition, the toxicity of CMGCZ about the heart, liver, spleen, lung and kidney was low to none (Fig. S12), and the weight of rats remained constant (Fig. S13). This appreciable biosafety was mainly because of a large and stable size of CMGCZ in the oral environment, which avoid complex entering the blood and causing organ injury.

## 4. Conclusion

In summary, we designed a glucose-driven transformable complex (CMGCZ) for synergistic therapeutics of diabetic periodontitis. The complex could scavenge glucose and produce gluconic acid, which causes the collapse of the core of CMGCZ. As the existence of residual hydrogel shell, the complex is transformed from inflexible to flexible, facilitating the complex overcome the steric hindrance of the diffusion-reaction inhibition of biofilm. The residual hydrogel shell also protected GOx/CAT from the static chelation and enzymatic degradation of the diffusion-reaction inhibition of biofilm. In the process of transformation, MINO is released sustainably for bacteria-killing through the whole layers of biofilm. In addition, the glucose-scavenging ability of CMGCZ could ameliorate the pyroptosis of macrophages to decrease the secretion of pro-inflammatory factors, thereby reducing inflamm-aging to alleviate the dysfunction of periodontal tissue. Therefore, the glucose-driven transformable complex (CMGCZ) paves the way for novel treatment options for diabetic periodontitis.

## 5. Associated content

### 5.1. Supplementary material

Supplementary material (The synthesis procedures of CMGCZ; SEM images of ZIF-8, CMGCZ and TEM images of CaAlg hydrogel shell; TEM images of ZIF-8; Enzyme recovery of GOx and CAT after encapsulation; The storage modulus and loss modulus of CMGCZ suspension; Injectability of CMGCZ; The penetrate ability of CMGCZ treated with different glucose concentrations in agar; The relation between the release of MINO and penetrated depth; Procedures of the establishment of dental plaque biofilm in vitro; The hemocompatibility of CMGCZ; Cell viability of macrophages exposed in various glucose concentration; The H & E images of heart, liver, spleen, lung and kidney harvested in rat model of each experimental group; Weight changes of rats in each CMGCZ group during the whole experiment) is available in the online version of this article.

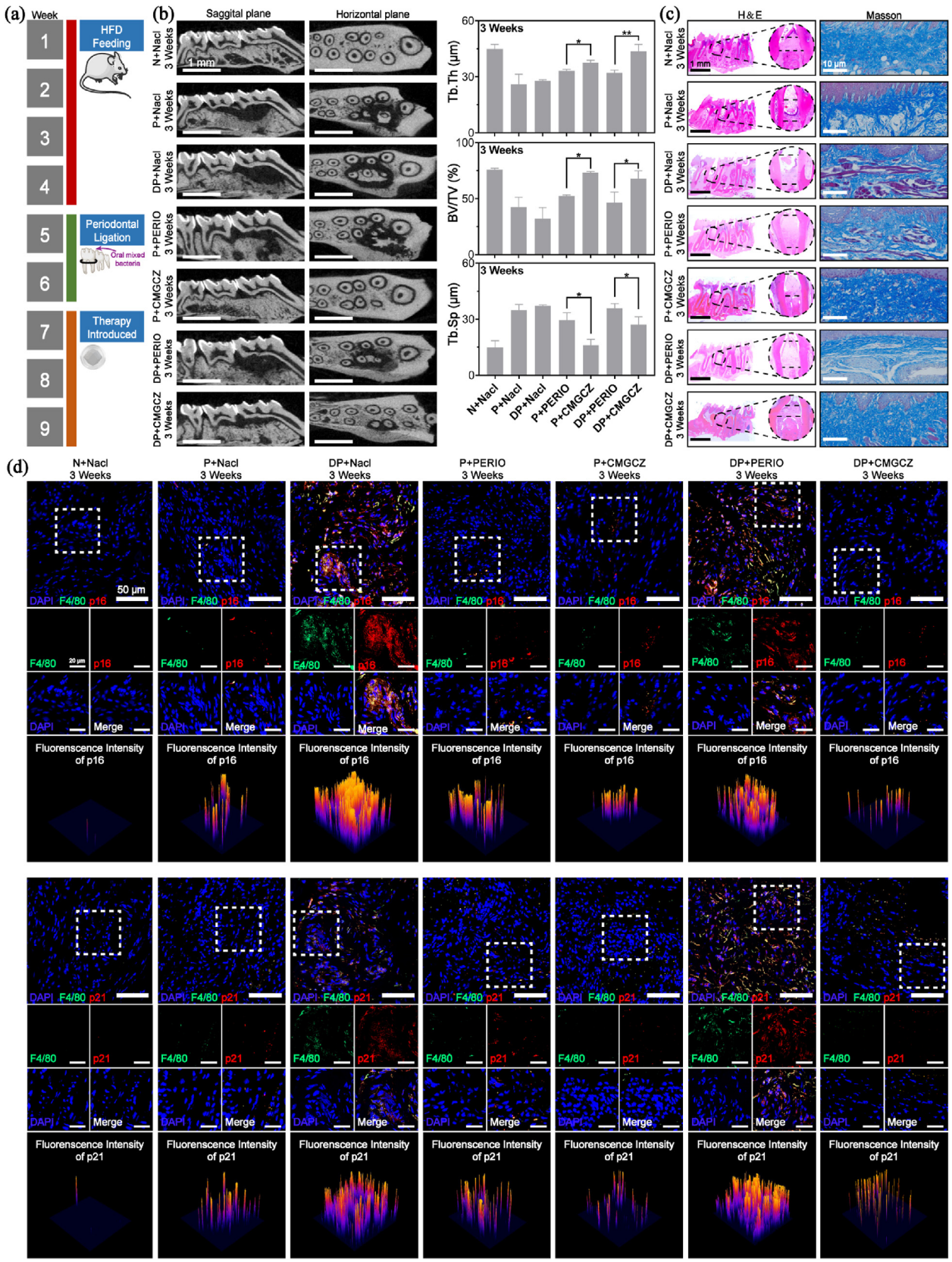


**Fig. 5.** Evaluation of periodontal therapeutic effect of CMGCZ in vivo. (a) Illustration of the establishment of diabetes and periodontitis model. (b) Micro-CT images of representative area of alveolar bone (scale bar: 1 mm). Tb. Sp, Tb·Th and BV/TV were determined by Bone-J plugins in Fiji (means ± SD, n = 3). * is $p < 0.05$, ** is $p < 0.01$. (c) The results of H & E (scale bar: 1 mm) and Masson staining (scale bar: 10 μm) of periodontal conditions in different groups. (d) Representative immunofluorescence images of p16, p21 and F4/80 in periodontal tissue of different groups (scale bar: 50 μm and 20 μm). Artwork in (a) was partially created with BioRender.com.

## Credit author statement

Rongbing Tang: Methodology, Investigation, Writing – original draft; Yanrong Ren: Methodology, Software, Investigation, Writing; Yueting Zhang: Methodology, Software, Investigation, Writing, Analysis, Visualization; Mengying Yin: Formal analysis, Visualization; Xinyu Ren: Methodology, Data curation; Qiangyuan Zhu: Methodology, Writing; Cen Gao: review/Visualization; Wei Zhang: Visualization; Guangxiu Liu: Writing – review & editing, Resources; Bin Liu: Writing – review & editing, Resources.

## Author contributions

[#]R. Tang, Y. Ren and Y. Zhang contributed equally to this work.

## Declaration of competing interest

The authors declare that they have no known competing financial interests or personal relationships that could have appeared to influence the work reported in this paper.

## Data availability

Data will be made available on request.

## Acknowledgment

This study was supported by the National Natural Science Foundation of China (82101011), the Fundamental Research Funds for the Central Universities (lzujbky-2022-ey19), Gansu Association for Science and Technology (GXH20220530-16), Natural Science Foundation of Gansu Province of China (20YF8WA084), Clinical Research Center for Oral Diseases, Gansu Province (20YF8FA073), the Scientific and Technological Foundation of Gansu Province (20JR10FA670), the open fund of Key Laboratory of Dental Maxillofacial Reconstruction and Biological Intelligence Manufacturing, Gansu Province (20JR10RA653 - ZDKF20210301), Hospital of Stomatology Lanzhou University Scientific Research Project (lzukqky-2021-q01, lzukqky-2021-q07).

## Appendix A. Supplementary data

Supplementary data to this article can be found online at https://doi.org/10.1016/j.mtbio.2023.100678.

## References

[1] N. Nwizu, J. Wactawski-Wende, R.J. Genco, Periodontal disease and cancer: epidemiologic studies and possible mechanisms, Periodontol 83 (1) (2000 2020) 213–233.
[2] J. Slots, Periodontitis: facts, fallacies and the future, Periodontol 75 (1) (2000 2017) 7–23.
[3] J. Slots, Primer on etiology and treatment of progressive/severe periodontitis: a systemic health perspective, Periodontol 83 (1) (2000 2020) 272–276.
[4] N.S. Jakubovics, S.D. Goodman, L. Mashburn-Warren, G.P. Stafford, F. Cieplik, The dental plaque biofilm matrix, Periodontol 86 (1) (2000 2021) 32–56.
[5] D.F. Kinane, P.G. Stathopoulou, P.N. Papapanou, Periodontal diseases, Nat. Rev. Dis. Prim. 3 (2017), 17038.
[6] H.C. Flemming, J. Wingender, The biofilm matrix, Nat. Rev. Microbiol. 8 (9) (2010) 623–633.
[7] D.E. Deas, A.J. Moritz, R.S. Sagun, S.F. Gruwell, C.A. Powell, Scaling and root planing vs. conservative surgery in the treatment of chronic periodontitis, Periodontol 71 (1) (2000 2016) 128–139.
[8] F. Graziani, D. Karapetsa, B. Alonso, D. Herrera, Nonsurgical and surgical treatment of periodontitis: how many options for one disease? Periodontol 75 (1) (2000 2017) 152–188.
[9] M. Zhou, X. Xu, J. Li, J. Zhou, Y. He, Z. Chen, S. Liu, D. Chen, H. Li, G. Li, J. Huang, G. Yang, T. Zhang, J. Song, C-reactive protein perturbs alveolar bone homeostasis: an experimental study of periodontitis and diabetes in the rat, J. Clin. Periodontol. 49 (10) (2022) 1052–1066.
[10] R.J. Genco, W.S. Borgnakke, Diabetes as a potential risk for periodontitis: association studies, Periodontol 83 (1) (2000 2020) 40–45.
[11] D. Polak, L. Shapira, An update on the evidence for pathogenic mechanisms that may link periodontitis and diabetes, J. Clin. Periodontol. 45 (2) (2018) 150–166.
[12] P. Zhang, Q. Wang, L. Nie, R. Zhu, X. Zhou, P. Zhao, N. Ji, X. Liang, Y. Ding, Q. Yuan, Q. Wang, Hyperglycemia-induced inflamm-aging accelerates gingival senescence via NLRC4 phosphorylation, J. Biol. Chem. 294 (49) (2019) 18807–18819.
[13] P. Zhao, Z. Yue, L. Nie, Z. Zhao, Q. Wang, J. Chen, Q. Wang, Hyperglycaemia-associated macrophage pyroptosis accelerates periodontal inflamm-aging, J. Clin. Periodontol. 48 (10) (2021) 1379–1392.
[14] Y. Qu, S. Misaghi, A. Izrael-Tomasevic, K. Newton, L.L. Gilmour, M. Lamkanfi, S. Louie, N. Kayagaki, J. Liu, L. Kömüves, J.E. Cupp, D. Arnott, D. Monack, V.M. Dixit, Phosphorylation of NLRC4 is critical for inflammasome activation, Nature 490 (7421) (2012) 539–542.
[15] M. Matusiak, N. Van Opdenbosch, L. Vande Walle, J.-C. Sirard, T.-D. Kanneganti, M. Lamkanfi, Flagellin-induced NLRC4 phosphorylation primes the inflammasome for activation by NAIP5, Proc. Natl. Acad. Sci. U. S. A. 112 (5) (2015) 1541–1546.
[16] C.L. Evavold, I. Hafner-Bratkovič, P. Devant, J.M. D'Andrea, E.M. Ngwa, E. Borsić, J.G. Doench, M.W. LaFleur, A.H. Sharpe, J.R. Thiagarajah, J.C. Kagan, Control of gasdermin D oligomerization and pyroptosis by the Ragulator-Rag-mTORC1 pathway, Cell 184 (17) (2021) 4495–4511.
[17] K. Wang, Q. Sun, X. Zhong, M. Zeng, H. Zeng, X. Shi, Z. Li, Y. Wang, Q. Zhao, F. Shao, J. Ding, Structural mechanism for GSDMD targeting by autoprocessed caspases in pyroptosis, Cell 180 (5) (2020) 941–955.
[18] K.C. Barnett, J.P.Y. Ting, Mitochondrial GSDMD pores DAMPen pyroptosis, Immunity 52 (3) (2020) 424–426.
[19] M. Karmakar, M. Minns, E.N. Greenberg, J. Diaz-Aponte, K. Pestonjamasp, J.L. Johnson, J.K. Rathkey, D.W. Abbott, K. Wang, F. Shao, S.D. Catz, G.R. Dubyak, E. Pearlman, N-GSDMD trafficking to neutrophil organelles facilitates IL-1β release independently of plasma membrane pores and pyroptosis, Nat. Commun. 11 (1) (2020) 2212.
[20] D. Shang, Y. Hong, W. Xie, Z. Tu, J. Xu, Interleukin-1β drives cellular senescence of rat astrocytes induced by oligomerized amyloid β peptide and oxidative stress, Front. Neurol. 11 (2020) 929.
[21] D.H. Kim, B. Lee, J. Lee, M.E. Kim, J.S. Lee, J.H. Chung, B.P. Yu, H.H. Dong, H.Y. Chung, FoxO6-mediated IL-1β induces hepatic insulin resistance and age-related inflammation via the TF/PAR2 pathway in aging and diabetic mice, Redox Biol. 24 (2019), 101184.
[22] M. Du, Y. Wang, Z. Liu, L. Wang, Z. Cao, C. Zhang, Y. Hao, H. He, Effects of IL-1β on MMP-9 expression in cementoblast-derived cell line and MMP-mediated degradation of type I collagen, Inflammation 42 (2) (2019) 413–425.
[23] R.P. Darveau, Periodontitis: a polymicrobial disruption of host homeostasis, Nat. Rev. Microbiol. 8 (7) (2010) 481–490.
[24] H.C. Flemming, J. Wingender, U. Szewzyk, P. Steinberg, S.A. Rice, S. Kjelleberg, Biofilms: an emergent form of bacterial life, Nat. Rev. Microbiol. 14 (9) (2016) 563–575.
[25] M. Okshevsky, R.L. Meyer, The role of extracellular DNA in the establishment, maintenance and perpetuation of bacterial biofilms, Crit. Rev. Microbiol. 41 (3) (2015) 341–352.
[26] S. Fulaz, S. Vitale, L. Quinn, E. Casey, Nanoparticle-biofilm interactions: the role of the EPS matrix, Trends Microbiol. 27 (11) (2019) 915–926.
[27] L. Karygianni, Z. Ren, H. Koo, T. Thurnheer, Biofilm matrixome: extracellular components in structured microbial communities, Trends Microbiol. 28 (8) (2020) 668–681.
[28] Z. Liu, F. Wang, J. Ren, X. Qu, A series of MOF/Ce-based nanozymes with dual enzyme-like activity disrupting biofilms and hindering recolonization of bacteria, Biomaterials 208 (2019) 21–31.
[29] M. Yin, J. Wu, M. Deng, P. Wang, G. Ji, M. Wang, C. Zhou, N.T. Blum, W. Zhang, H. Shi, N. Jia, X. Wang, P. Huang, Multifunctional magnesium organic framework-based microneedle patch for accelerating diabetic wound healing, ACS Nano 15 (11) (2021) 17842–17853.
[30] Z. Li, H. Li, L. Zhao, X. Liu, C. Wan, Understanding the role of cations and hydrogen bonds on the stability of aerobic granules from the perspective of the aggregation and adhesion behavior of extracellular polymeric substances, Sci. Total Environ. 795 (2021), 148659.
[31] W. Liang, P. Wied, F. Carraro, C.J. Sumby, B. Nidetzky, C.-K. Tsung, P. Falcaro, C.J. Doonan, Metal-organic framework-based enzyme biocomposites, Chem. Rev. 121 (3) (2021) 1077–1129.
[32] D. Wang, D. Jana, Y. Zhao, Metal-organic framework derived nanozymes in biomedicine, Acc. Chem. Res. 53 (7) (2020) 1389–1400.
[33] F. Carraro, J.D. Williams, M. Linares-Moreau, C. Parise, W. Liang, H. Amenitsch, C. Doonan, C.O. Kappe, P. Falcaro, Continuous-flow synthesis of ZIF-8 biocomposites with tunable particle size, Angew Chem. Int. Ed. Engl. 59 (21) (2020) 8123–8127.
[34] M. Xu, Y. Hu, W. Ding, F. Li, J. Lin, M. Wu, J. Wu, L.-P. Wen, B. Qiu, P.-F. Wei, P. Li, Rationally designed rapamycin-encapsulated ZIF-8 nanosystem for overcoming chemotherapy resistance, Biomaterials 258 (2020), 120308.
[35] J. Shen, M. Ma, M. Shafiq, H. Yu, Z. Lan, H. Chen, Microfluidics-assisted engineering of pH/Enzyme dual-activatable ZIF@polymer nanosystem for co-delivery of proteins and chemotherapeutics with enhanced deep-tumor penetration, Angew Chem. Int. Ed. Engl. 61 (14) (2022), e202113703.
[36] W.-H. Chen, G.-F. Luo, M. Vázquez-González, R. Cazelles, Y.S. Sohn, R. Nechushtai, Y. Mandel, I. Willner, Glucose-responsive metal-organic-framework nanoparticles act as "smart" sense-and-treat Carriers, ACS Nano 12 (8) (2018) 7538–7545.
[37] C. Zhang, S. Hong, M.-D. Liu, W.-Y. Yu, M.-K. Zhang, L. Zhang, X. Zeng, X.-Z. Zhang, pH-sensitive MOF integrated with glucose oxidase for glucose-responsive insulin delivery, J. Contr. Release 320 (2020) 159–167.

[38] M. Wang, X. Zhou, Y. Li, Y. Dong, J. Meng, S. Zhang, L. Xia, Z. He, L. Ren, Z. Chen, X. Zhang, Triple-synergistic MOF-nanozyme for efficient antibacterial treatment, Bioact. Mater. 17 (2022) 289–299.
[39] Y. Du, X. Jia, L. Zhong, Y. Jiao, Z. Zhang, Z. Wang, Y. Feng, M. Bilal, J. Cui, S. Jia, Metal-organic frameworks with different dimensionalities: an ideal host platform for enzyme@ MOF composites, Coord. Chem. Rev. 454 (2022), 214327.
[40] X. Shen, Y. Du, Z. Du, X. Tang, P. Li, J. Cheng, R. Yan, J. Cui, Construction of enzyme@glutathione hybrid metal-organic frameworks: glutathione-boosted microenvironment fine-tuning of biomimetic immobilization for improving catalytic performance, Mater. Today Chem. 27 (2023), 101326.
[41] Y. Feng, H. Hu, Z. Wang, Y. Du, L. Zhong, C. Zhang, Y. Jiang, S. Jia, J. Cui, Three-dimensional ordered magnetic macroporous metal-organic frameworks for enzyme immobilization, J. Colloid Interface Sci. 590 (2021) 436–445.
[42] Z. Wang, Y. Liu, J. Li, G. Meng, D. Zhu, J. Cui, S. Jia, Efficient immobilization of enzymes on amino functionalized MIL-125-NH2 metal organic framework, Biotechnol. Bioproc. Eng. 27 (1) (2022) 135–144.
[43] Y. Feng, Y. Du, G. Kuang, L. Zhong, H. Hu, S. Jia, J. Cui, Hierarchical micro-and mesoporous ZIF-8 with core–shell superstructures using colloidal metal sulfates as soft templates for enzyme immobilization, J. Colloid Interface Sci. 610 (2022) 709–718.
[44] J. Troyano, A. Carné-Sánchez, C. Avci, I. Imaz, D. Maspoch, Colloidal metal-organic framework particles: the pioneering case of ZIF-8, Chem. Soc. Rev. 48 (23) (2019) 5534–5546.
[45] W. Zhang, Y. Zhou, Y. Fan, R. Cao, Y. Xu, Z. Weng, J. Ye, C. He, Y. Zhu, X. Wang, Metal-organic-framework-based hydrogen-release platform for multieffective helicobacter pylori targeting therapy and intestinal flora protective capabilities, Adv Mater 34 (2) (2022), e2105738.
[46] Y. Yan, M. Ni, F. Wang, Y. Yu, X. Gong, Y. Huang, W. Tao, C. Li, F. Wang, Metal-organic framework-based biosensor for detecting hydrogen peroxide in plants through Color-to-thermal signal conversion, ACS Nano 16 (9) (2022) 15175–15187.
[47] F. Li, T. Chen, F. Wang, J. Chen, Y. Zhang, D. Song, N. Li, X.-H. Lin, L. Lin, J. Zhuang, Enhanced cancer starvation therapy enabled by an autophagy inhibitors-encapsulated biomimetic ZIF-8 nanodrug: disrupting and harnessing dual pro-survival autophagic responses, ACS Appl. Mater. Interfaces 14 (19) (2022) 21860–21871.
[48] L.H. Fu, Y. Wan, C. Qi, J. He, C. Li, C. Yang, H. Xu, J. Lin, P. Huang, Nanocatalytic theranostics with glutathione depletion and enhanced reactive oxygen species generation for efficient cancer therapy, Adv. Mater. 33 (7) (2021), 2006892.
[49] S.H. Ching, N. Bansal, B. Bhandari, Alginate gel particles–A review of production techniques and physical properties, Crit. Rev. Food Sci. Nutr. 57 (6) (2017) 1133–1152.
[50] Y. Zhang, Z. Xie, Z. Wang, X. Feng, Y. Wang, A. Wu, Unveiling the adsorption mechanism of zeolitic imidazolate framework-8 with high efficiency for removal of copper ions from aqueous solutions, Dalton Trans. 45 (32) (2016) 12653–12660.
[51] W. She, K. Luo, C. Zhang, G. Wang, Y. Geng, L. Li, B. He, Z. Gu, The potential of self-assembled, pH-responsive nanoparticles of mPEGylated peptide dendron-doxorubicin conjugates for cancer therapy, Biomaterials 34 (5) (2013) 1613–1623.
[52] H. Wang, X. Chang, Q. Ma, B. Sun, H. Li, J. Zhou, Y. Hu, X. Yang, J. Li, X. Chen, Bioinspired drug-delivery system emulating the natural bone healing cascade for diabetic periodontal bone regeneration, Bioact. Mater. 21 (2023) 324–339.
[53] W. Zhong, X. Wang, L. Yang, Y. Wang, Q. Xiao, S. Yu, R.D. Cannon, Y. Bai, C. Zhang, D. Chen, P. Ji, X. Gao, J. Song, Nanocarrier-assisted delivery of metformin boosts remodeling of diabetic periodontal tissue via cellular exocytosis-mediated regulation of endoplasmic reticulum homeostasis, ACS Nano 16 (11) (2022) 19096–19113.
[54] Y. Ihara, T. Takeshita, S. Kageyama, R. Matsumi, M. Asakawa, Y. Shibata, Y. Sugiura, K. Ishikawa, I. Takahashi, Y. Yamashita, Identification of initial colonizing bacteria in dental plaques from young adults using full-length 16S rRNA Gene Sequencing, mSystems 4 (5) (2019), e00360, 19.
[55] Z. Wang, Y. Shen, M. Haapasalo, Dynamics of dissolution, killing, and inhibition of dental plaque biofilm, Front. Microbiol. 11 (2020) 964.
[56] W. Zhong, X. Wang, L. Yang, Y. Wang, Q. Xiao, S. Yu, R.D. Cannon, Y. Bai, C. Zhang, D. Chen, Nanocarrier-Assisted delivery of metformin boosts remodeling of diabetic periodontal tissue via cellular exocytosis-mediated regulation of endoplasmic reticulum homeostasis, ACS Nano 16 (11) (2022) 19096–19113.
[57] R. Kumari, P. Jat, Mechanisms of cellular senescence: cell cycle arrest and senescence associated secretory phenotype, Front. Cell Dev. Biol. 9 (2021), 645593.
[58] L. Zhang, Y. Wang, C. Wang, M. He, J. Wan, Y. Wei, J. Zhang, X. Yang, Y. Zhao, Y. Zhang, Light-activable on-demand release of nano-antibiotic platforms for precise synergy of thermochemotherapy on periodontitis, ACS Appl. Mater. Interfaces 12 (3) (2019) 3354–3362.